nature catalysis

ARTICLES

https://doi.org/10.1038/s41929-019-0225-7

Efficient electrocatalytic conversion of carbon monoxide to propanol using fragmented copper

Yuanjie Pang[1,2,3,6], Jun Li[1,2,6], Ziyun Wang[2], Chih-Shan Tan[2], Pei-Lun Hsieh[4], Tao-Tao Zhuang[2], Zhi-Qin Liang[2], Chengqin Zou[2], Xue Wang[2], Phil De Luna[5], Jonathan P. Edwards[1], Yi Xu[1], Fengwang Li[2], Cao-Thang Dinh[2], Miao Zhong[2], Yuanhao Lou[3], Dan Wu[3], Lih-Juann Chen[4], Edward H. Sargent[2*] and David Sinton[1*]

The renewable-energy-powered electrocatalytic conversion of carbon dioxide and carbon monoxide into carbon-based fuels provides a means for the storage of renewable energy. We sought to convert carbon monoxide—an increasingly available and low-cost feedstock that could benefit from an energy-efficient upgrade in value—into *n*-propanol, an alcohol that can be directly used as engine fuel. Here we report that a catalyst consisting of highly fragmented copper structures can bring C_1 and C_2 binding sites together, and thereby promote further coupling of these intermediates into *n*-propanol. Using this strategy, we achieved an *n*-propanol selectivity of 20% Faradaic efficiency at a low potential of −0.45 V versus the reversible hydrogen electrode (ohmic corrected) with a full-cell energetic efficiency of 10.8%. We achieved a high reaction rate that corresponds to a partial current density of 8.5 mA cm^{-2} for *n*-propanol.

The electrochemical conversion of carbon dioxide (CO_2) into carbon-based feedstocks and fuels is a promising method for the long-term storage of renewable electricity. At present, the electrochemical carbon dioxide reduction reaction (CO_2RR) has achieved high efficiencies and reaction rates to produce C_1 chemicals, including carbon monoxide (CO)[1–5] and formate ($HCOO^-$) (refs. [6–9]). The efficiencies and reaction rates for the production of C_2 chemicals, including ethylene[10–14] and ethanol[13,14], are improving fast; however, the efficient production of higher-value C_3 chemicals has yet to be demonstrated. Of the C_3 chemicals that have been reported as CO_2RR products, including *n*-propanol, propionaldehyde, allyl alcohol, acetone and hydroxyacetone, *n*-propanol has to date exhibited the highest selectivity[15,16]. Of particular interest, *n*-propanol is a C_3 product that can be directly used as a fuel: it has an impressive energy–mass density (30.94 kJ/g) and a high research octane number (118)[17], which offers one avenue to the decarbonization of mobile vehicle fuels.

Copper-based materials have been found to be the only efficient CO_2RR electrocatalyst for *n*-propanol. Hori et al. reported *n*-propanol as a CO_2RR product on a copper electrode with a Faradaic efficiency of 4.2% under a potential of −1.4 V versus the normal hydrogen electrode[18]. More recently, the Faradaic efficiency for *n*-propanol production from CO_2RR was enhanced via the optimization of copper-based catalysts[19–23], which include morphologically reconstructed copper nanoparticles[19], grain boundary control[20], two-step activation[21], metal ion cycling[22] and core–shell structures[23], which brings the *n*-propanol Faradaic efficiency to 15% at a potential of −0.96 V versus the reversible hydrogen electrode (RHE)[22].

Using CO instead of CO_2 as the feedstock for electrochemical *n*-propanol production provides a means to enhance surface-adsorbed CO species, an intermediate for carbon–carbon coupling[24–26]. Exploring the carbon monoxide reduction reaction (CORR) is timely in light of the comparatively mature electrochemical CO_2 to CO conversion[1–5], and the relative abundance of concentrated waste streams of CO from the steel industry[27]. Early studies of CORR performed in H cells reported *n*-propanol as a product[28–31], with oxide-derived copper material that attained an *n*-propanol selectivity of 10% Faradaic efficiency at a potential of −0.4 V versus RHE[28]. Using a flow cell in combination with a gas diffusion electrode (GDE) with the CO mass transport limitation removed, the *n*-propanol Faradaic efficiency was improved to above 20% (refs. [32–34]).

The complete reaction pathway of C_3 production requires further investigation, and the efficiency may be dependent on the Cu oxidation states[21] and grain boundaries[29,35]. However, it was proposed[20] that a critical step in *n*-propanol formation is the coupling between two surface-adsorbed intermediates: a C_1 and a C_2 species. It is also established that these two intermediates are preferentially stabilized on different sites on the Cu surface: the Cu(111) facet is C_1 selective whereas the Cu(100) facet is C_2 selective[16,24,36].

With this in mind, we took the view that the design of a highly C_3-selective catalyst could beneficially target a mixture of Cu(111) and Cu(100) facets, which could create additional opportunities for C_1 and C_2 intermediates to become coupled. We therefore performed simulations to examine the influence of the Cu(111) and Cu(100) interfacial region, and pursued the realization of catalysts that exhibit a high degree of distinct facet fragments. As a result, we demonstrated a CORR with a 20% Faradaic efficiency for *n*-propanol at a low potential of −0.45 V versus RHE (corrected for ohmic loss (*iR* corrected), 0.65 V overpotential). We used transmission electron microscopy (TEM) to correlate this performance relative to that of less fragmented controls.

[1]Department of Mechanical and Industrial Engineering, University of Toronto, Toronto, ON, Canada. [2]Department of Electrical and Computer Engineering, University of Toronto, Toronto, ON, Canada. [3]School of Optical and Electronic Information, Huazhong University of Science and Technology, Wuhan, Hubei, China. [4]Department of Materials Science and Engineering, National Tsing Hua University, Hsinchu, Hsinchu, Taiwan. [5]Department of Materials Science and Engineering, University of Toronto, Toronto, ON, Canada. [6]These authors contributed equally: Yuanjie Pang and Jun Li. *e-mail: ted.sargent@utoronto.ca; sinton@mie.utoronto.ca

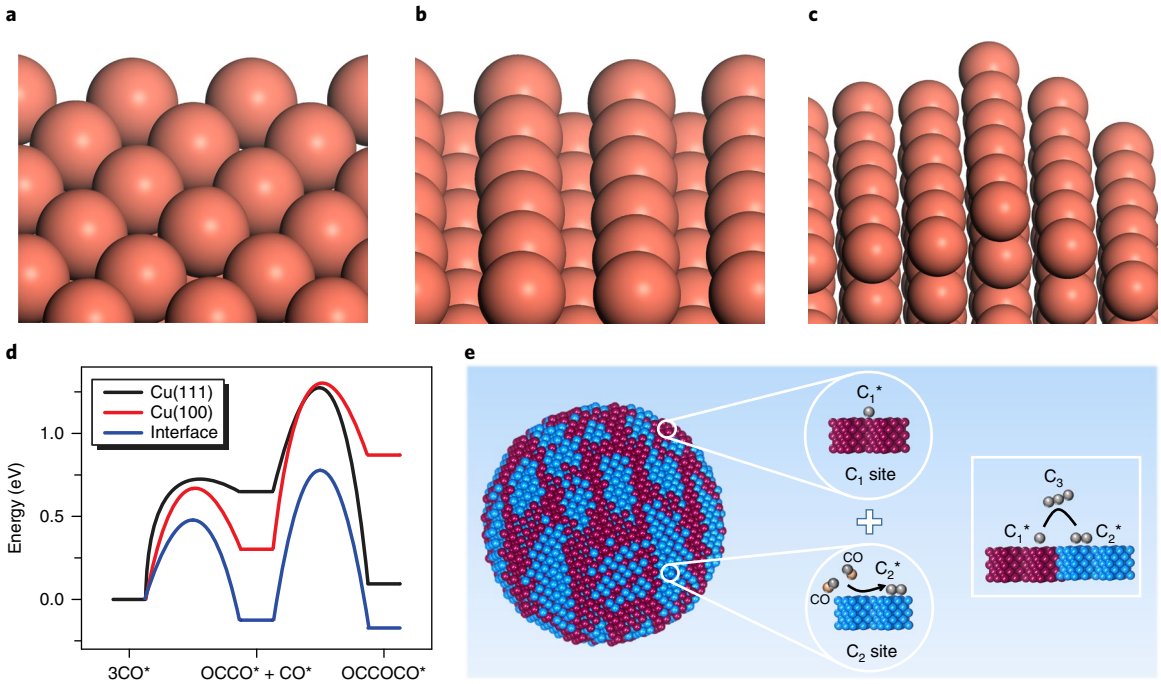

Fig. 1 | DFT calculation results for C_1, C_2 and C_3. a–c, Geometries of Cu(111) (**a**), Cu(100) (**b**) and the interface between Cu(111) and Cu(100) (**c**). **d**, The energy profiles of CO–CO and CO–OCCO dimerization on Cu(111), Cu(100) and the interface. **e**. Catalyst with highly mixed nanofragments of the Cu(200) and Cu(111) facets may bring the optimal C_1 and C_2 sites into physical proximity, contributing with one another to the coupling of C_1–C_2 and then the coupling into C_3 products.

Results

Density functional theory calculations. CO reduction to C_3 products first requires a C_1–C_1 coupling step, followed by a C_1–C_2 coupling step. CO dimerization is suggested to be one of the main C_1–C_1 coupling pathways to form OCCO (refs. [37,38]). The mechanism for C_1–C_2 coupling is less established. In CO reduction, the CO species is abundant on the surface, and thus coupling between CO and OCCO is a likely pathway, as suggested in previous work[23]. Here we applied density functional theory (DFT) calculations to assess the CO dimerization and CO–OCCO coupling on the Cu(111) and Cu(100) facets, as well as the interfaces among these facets (Fig. 1a–c and Supplementary Figs. 1–6).

CO–CO dimerization is more favourable on Cu(100), both thermodynamically and kinetically, compared to that on Cu(111) (Fig. 1d). Thus, the coverage of C_2 on Cu(100) is expected to be higher than that on Cu(111). However, C_3 formation is slow on Cu(100) because the energy barrier and enthalpy change of the further C_1–C_2 coupling on Cu(100) are a relatively high 1 eV and 0.57 eV, respectively (Supplementary Table 1).

Combining Cu(111) and Cu(100) is a promising approach to take the advantage of active sites on both facets. We modelled the interface between Cu(111) and Cu(100) (Fig. 1c) and found that it lowers the barriers of both the CO–CO and CO–OCCO coupling steps compared to the individual facets (Fig. 1d), which promotes C_3 production. Furthermore, due to differing coverages on Cu(111) and Cu(100), the interface also serves to collocate C_1 and C_2, which further increases the rate of C_1–C_2 coupling (Fig. 1e).

Materials synthesis and electrode preparation. We set out therefore to design a Cu-based catalyst with a highly fragmented structure for CORR experiments. We first synthesized a precatalyst that consisted of copper oxide (CuO). We used a cuprous salt (copper (I) iodide (CuI)) precursor, which is less reactive than cupric salts, to slow the nucleation and growth rates, and this allowed the generation of a variety of crystalline phases[39]. The precatalyst was then deposited onto a GDE and in situ reduced to Cu during CORR. We show below that this produces a highly fragmented copper (HF-Cu) material.

The chemical composition of the precatalyst is CuO, as confirmed using X-ray diffraction (XRD) (Fig. 2a) and X-ray absorption spectroscopy (XAS) (Fig. 2b). To study the effect of crystalline structure on *n*-propanol selectivity, we chose control samples with the same chemical composition (CuO) but that offered different crystalline structures. As a first control, we modulated the crystalline structure of the as-synthesized CuO precatalyst by annealing it in an argon atmosphere under 500 °C for two hours. As a second control, we used a commercial 40 nm CuO nanoparticle as the precatalyst. We show here that these control precatalysts result in medium- and low-fragmented copper (MF-Cu and LF-Cu, respectively) structures during CORR. Scanning electron microscopy (SEM) images (Fig. 2c–e) show that all the precatalysts have the morphology of multidispersed nanoparticles. The chemical compositions of the controls were also determined to be CuO using XRD (Fig. 2a). X-ray photoelectron spectroscopy confirmed that negligible iodine remains in the precatalyst (0.6%) (Supplementary Fig. 7), which rules out iodine as a significant contributor to the CORR mechanism here[40].

To overcome the low solubility of CO and ensure an abundant CO supply to the catalyst surface, we utilized an electrochemical flow cell that employed a GDE[32–34,41]. The flow cell provided a superior mass transport of CO, and allow performance testing at the high current densities relevant to industrial processes. Potassium hydroxide (KOH) solution at 1 M was used as the electrolyte throughout this work. The precatalysts were ground, suspended into a colloidal solution and then airbrushed onto a GDE (Methods).

Figure 2f–k shows SEM and TEM images of the Cu catalysts with varying degrees of fragmentation after 30 minutes of CORR. The morphology of each catalyst remained largely unchanged during

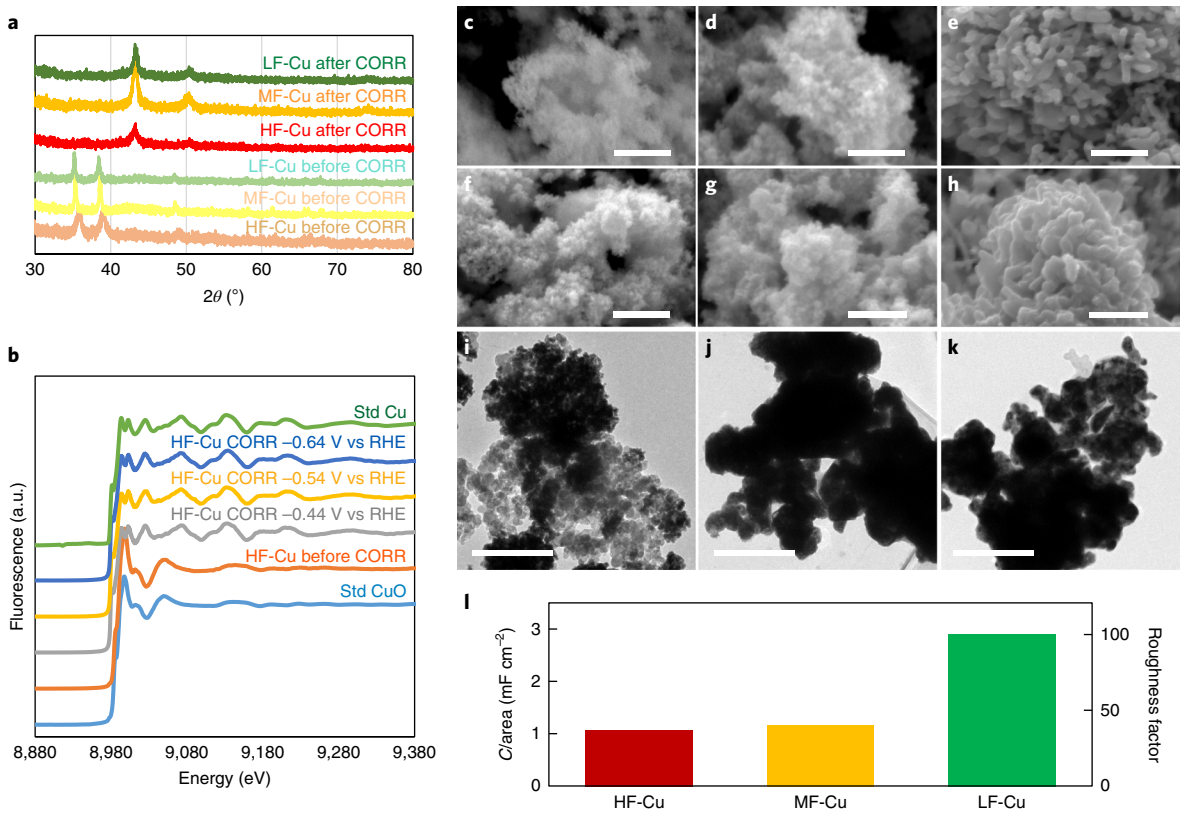

Fig. 2 | Materials characterization. a, XRD of the precatalysts and catalysts. **b**, Operando XAS of the HF-Cu catalysts at different applied potentials in comparison with XAS of commercial standard (Std) Cu and CuO. **c**–**k**, SEM (**c**–**h**) and TEM (**i**–**k**) of various samples. **c**–**e**, SEM of the three precatalysts. **f**–**h**, SEM of the HF-Cu (**f**), MF-Cu (**g**) and LF-Cu (**h**) catalysts after CORR. **i**–**k**, TEM of the HF-Cu (**i**), MF-Cu (**j**) and LF-Cu (**k**) catalysts after CORR. **l**, The electrochemical surface area was measured via the electric double layer capacitance (*C*), and the roughness factor was calculated by defining the surface roughness of electropolished polycrystalline Cu as 1 (with an electric double layer capacitance of 29 μF) (ref. [28]). a.u., arbitrary units; all scale bars, 500 nm.

CORR. To assess the surface roughness of different catalysts during the reaction, we measured the electric double layer capacitance after the CORR, and acquired cyclic voltammetry scans at different scan rates (Methods and Supplementary Fig. 8). As summarized in Fig. 2l, no correlation was found between surface roughness and the degree of lattice fragmentation of the three samples: the HF-Cu did not have an advantage over the others in surface roughness. All the catalysts consisted of Cu, as confirmed by XRD after the CORR (Fig. 2a). Operando XAS also confirmed that the HF-Cu electrode featured a characteristic spectrum of pristine Cu during CORR (Fig. 2b).

Crystalline structure characterization. We then investigated the crystalline structure of HF-Cu relative to the control catalysts. We first performed dark-field transmission electron microscopy (DF-TEM) imaging. This revealed the Cu(111) and Cu(200) facets (the latter is equivalent to Cu(100)) of the catalysts after CORR (Fig. 3a–c and Supplementary Figs. 9–11). We quantified the size of each fragment (delineated in Fig. 3a–c with red lines) with a continuous lattice in the catalyst. Supplementary Fig. 12a shows histograms of the fragment sizes of all the samples. Samples HF-Cu and MF-Cu comprised mostly fragments below 200 nm^2, whereas sample LF-Cu exhibited a significant portion of fragments larger than 400 nm^2. The full distribution histogram of fragment sizes for all the samples is provided in Supplementary Fig. 12b. The HF-Cu catalyst solely comprised fragments smaller than 700 nm^2. The MF-Cu catalyst had a noticeably decreased portion of fragments in the 300–700 nm^2 range, but an increased portion in the 800–1,000 nm^2 range. The LF-Cu catalyst has the least area that comprised small fragments (<300 nm^2), and the greatest area that comprised large fragments (≥1,000 nm^2). Additional details of the fragment size statistics for the three sample families are given in Supplementary Table 2, which shows that the HF-Cu catalyst has the smallest, and the LF-Cu the largest, mean and median in fragment sizes.

To resolve different facets and their spatial arrangements in each catalyst, we imaged the samples using high-resolution TEM (HR-TEM). The HF-Cu catalyst displayed a large density of fragments of Cu(100) (outlined in cyan in Fig. 3d–f) and Cu(111) (outlined in red) facets that are adjacent. The interface between the two facets that is expected to favour the C_1–C_2 intermolecular coupling is outlined in yellow in Fig. 3d. As selected area electron diffraction cannot be applied for areas as small as the facet fragments here, we obtained fast Fourier transforms (FFTs) for the facet fragments (Supplementary Fig. 13; typical FFTs are shown in Fig. 3d). The MF-Cu catalyst also exhibits Cu(100) and Cu(111) facets (Fig. 3e), but these facets are larger and more disperse and they create less interface compared to HF-Cu. The LF-Cu shows the largest facet fragment sizes of all the catalysts, with very few instances of adjacent Cu(100) and Cu(111). (Supplementary Figs. 13–31 give additional HR-TEM images of all the samples and Supplementary Fig. 32 gives the statistics of the (111):(100) interface length, normalized to sample areas, for all samples.)

To challenge further the existence and distribution of different facets on different catalysts in atomic resolution, we performed scanning transmission electron microscopy (STEM) in bright-field (BF) or annular dark field (ADF) modes. In the STEM, we looked

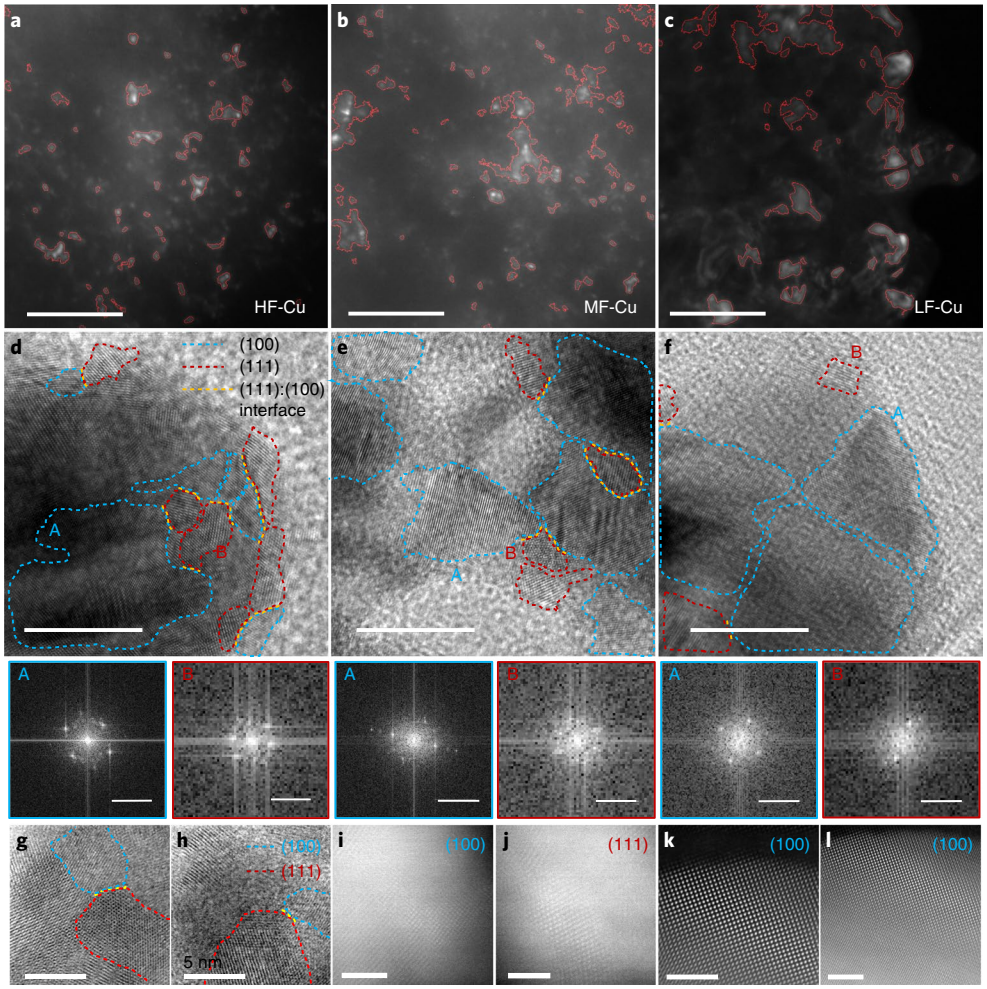

Fig. 3 | TEM imaging of crystalline structure of all the samples. a–c, The DF-TEM images highlight the Cu(111) and Cu(100) facets of catalysts HF-Cu (**a**), MF-Cu (**b**) and LF-Cu (**c**). Scale bars: 100 nm. **d–f**, The HR-TEM images show facet information for the catalysts HF-Cu (**d**), MF-Cu (**e**) and LF-Cu (**f**). As visual aids, cyan and red dotted lines circle fragments of the Cu(200) and Cu(111) facets, respectively, and yellow dotted lines highlight the interfaces between the (100) and (111) facets. HR-TEM scale bars, 10 nm. Below each HRTEM image, FFTs of two typical areas are shown, one for the (111) facet (A) and the other for the (100) facet (B). FFT scale bars, 10 nm^{-1}. **g–l**, BF-STEM and ADF-STEM images with atomic resolution of the catalysts HF-Cu (**g** and **h**), MF-Cu (**i** and **j**) and LF-Cu (**k** and **l**). The Cu(100) and Cu(111) facets on each sample are highlighted. STEM scale bars, 5 nm (**g** and **h**); 2 nm (**i–l**).

for characteristic regions that resemble the Cu(100) and Cu(111) fragments in the HR-TEM images and performed atomic microscopy for these regions. In agreement with the HR-TEM, the HF-Cu (Fig. 3g,h and Supplementary Fig. 33) and the MF-Cu (Fig. 3i,j and Supplementary Fig. 34) are seen to have a mixture of Cu(100) and Cu(111) facets. The Cu(111):(100) interfaces are clear on the HF-Cu surface. In comparison, the LF-Cu displays a largely uniform Cu(100) facet (Fig. 3k,l and Supplementary Fig. 35). Although this result does not rule out the existence of the Cu(111) facet on LF-Cu, it can be concluded that the Cu(100) and Cu(111) facets are further separated compared to the HF-Cu and MF-Cu catalysts. XRD (Fig. 2a) of all three catalysts shows a similar relative peak intensity for Cu(111) ($2\theta \approx 43°$) and Cu(200) (equivalent facet of Cu(100) ($2\theta \approx 51°$)), which indicates a similar facet combination in the three catalysts. The central differences in these catalysts are in the facet fragment sizes and the interfacial lengths that result from their distribution.

Taken together, the TEM studies indicate that the catalyst with the most fragmented crystalline structure, HF-Cu, presents an abundance of sites where the Cu(100) and Cu(111) facets conjoin, which may offer an advantage in forming C_3 products.

Electrocatalytic performance. We then investigated the CORR performance of the three sample types, all under identical CORR system conditions. We quantified the liquid phase products (*n*-propanol, ethanol and acetates) using NMR spectroscopy and the gas phase products using gas chromatography with a flame ionization detector (for hydrocarbon gases) and a thermal conductivity detector (for hydrogen). Figure 4a shows the Faradaic efficiency for each product produced by HF-Cu under various applied potentials. The only C_3 product detected, *n*-propanol, emerged at an onset potential of −0.35 V versus RHE (an overpotential of 0.55 V, *iR* corrected (Methods)) and exhibited a maximum Faradaic efficiency of 20.3 ± 0.1% at −0.45 V versus RHE (overpotential 0.65 V, *iR* corrected). The full-cell electrical power-to-chemical energy conversion efficiency (PCE) of this system for *n*-propanol was 10.8%. The partial current density (normalized to the geometric area of the GDE) for *n*-propanol production ($J_{n\text{-PrOH}}$) at this potential was 8.5 ± 1 mA cm^{-2} (Supplementary Fig. 36a,b). The HF-Cu catalyst produced the highest electrochemical-surface-area-normalized current densities for *n*-propanol, which indicates the highest intrinsic activity (Supplementary Fig. 36c,d).

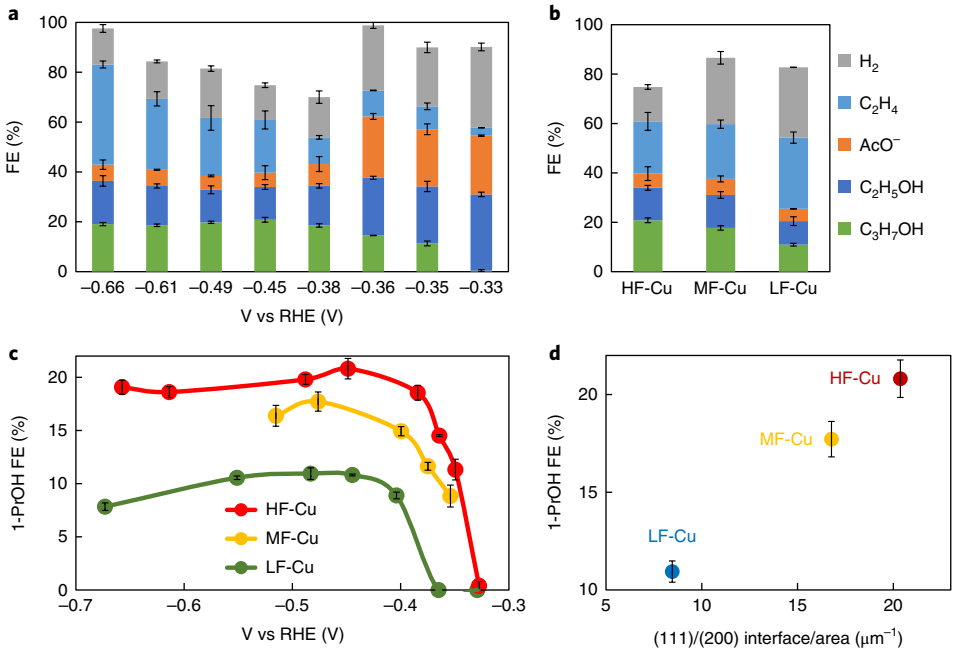

Fig. 4 | Catalyst performance in a CORR flow cell. a, Faradaic efficiencies (FE) for different products produced by HF-Cu under a range of potentials. **b**, Comparison of Faradaic efficiencies of different products produced by all three catalysts under potentials at which the maximum FE for *n*-propanol is reached. **c**, Comparisons of Faradaic efficiencies of *n*-propanol (1-Pr(OH)) produced by all three samples under a range of potentials. Curves that link the data points are guides to the eye. All potentials are *iR* corrected. **d**, The Cu(111):(100) interface per area, measured from the HR-TEM images of each sample, plotted against the *n*-propanol selectivity performance. Error bars represent s.d. from at least two measurements. The data are provided in Supplementary Data 1.

The high Faradaic efficiency for *n*-propanol spans a wide potential window, maintaining a selectivity of 19 ± 0.7% at a potential as high as −0.66 V (*iR* corrected) versus RHE. The C_2 (ethylene, ethanol and acetates) production window spans −0.34 V to −0.66 V versus RHE. The wide potential window for a high C_3 selectivity is in contrast with previous reports, which include electrosynthesis of *n*-propanol using CO_2RR (refs. [18–23]) or CORR (refs. [28–31]). We offer two contributing factors: (1) the flow cell electrolyser provides an abundant CO reagent at the catalyst surface and (2) the lattice-fragment-promoted C_1–C_2 coupling effect persists at a high potential, and so maintains a competitive C_3 selectivity. Maintaining a high selectivity at a high potential enables the desired fast *n*-propanol production; the maximum $J_{n\text{-PrOH}}$ achieved in this work is 33 ± 0.6 mA cm^{-2} (Supplementary Fig. 36). The high Faradaic efficiency for *n*-propanol was maintained for 70 minutes and dropped to 17.7 ± 0.4% over the following 130 minutes (Supplementary Fig. 37), probably due to the flooding of the electrolyte onto the gas side of the GDE[13].

The HF-Cu catalyst achieves the highest *n*-propanol selectivity observed in this work. In contrast, catalysts with a lower degree of lattice fragmentation show a lower selectivity to *n*-propanol. Compared in Fig. 4b,c and Supplementary Fig. 38a,b, samples MF-Cu and LF-Cu exhibit maximum Faradaic efficiency values of 17.5 and 11.5%. The trend of experimental *n*-propanol selectivity of the samples is in agreement with the density of Cu(111):(100) facet interface (Fig. 4d). Sample LF-Cu not only exhibited a lower Faradaic efficiency, but also a higher (more negative) onset potential for *n*-propanol. A similar trend of C_3 selectivity was also observed in the electroreduction of CO_2 using the three catalysts (Supplementary Fig. 39). Two additional controls, (1) a commercial 18 nm cuprous oxide (Cu_2O) nanoparticle and (2) a thermally evaporated 200 nm Cu layer on the Freudenberg gas diffusion layer, were also tested, and they both showed a low *n*-propanol selectivity, as summarized in Supplementary Fig. 40.

Discussion

We first consider whether the high *n*-propanol selectivity observed here may be due to the presence of oxide. The remaining Cu^+ or Cu^{2+} states in the catalyst during CORR or CO_2RR have shown propensity for C–C coupling[10,11,28]. However, the HF-Cu catalyst was completely reduced to Cu within the first 15 minutes of CORR, as confirmed using *operando* XAS (Fig. 2b). The reduction of the catalysts to pristine Cu after CORR is further supported by XRD (Fig. 2a). The catalysts investigated in this work did not show measurable Cu^+ or Cu^{2+} states in CORR within the limits of the signal-to-noise ratio available in the bulk-sensitive (Supplementary Fig. 41) operando XAS and XRD studies. We note that at the catalyst surface a trace amount of oxygen might remain beyond the detection limit of these tools. However, this amount is very small compared to that observed using similar characterizations in reports that focus on tuning selectivity using oxidation states[10,11]. On this basis, we conclude that the Cu oxide is reduced to the extent that any trace of oxygen remaining in the catalyst would not play a significant role in the performance.

Second, with respect to grain boundaries, the HF-Cu structure resembles the dense grain boundary structures that have exhibited enhanced CO_2RR[42] and CORR[28,35] performances. In previous reports, strain induced by the grain boundaries was found to be the key factor to account for an enhanced CO_2RR performance[42]. To assess strain in our material, we examined the Cu K-edge extended X-ray absorption fine structure (XAFS) using operando techniques. The results (Supplementary Fig. 42) show that the Cu local environment (that is, coordination and strain) of the HF-Cu catalyst was the same as that of the Cu foil standard. We therefore point again to C_1–C_2 coupling at boundaries among the different facets on the HF-Cu surface in a manner not reliant on strains.

In conclusion, lattice fragmentation engineering and randomization enabled us to achieve the electrocatalytic conversion of CO into

a C_3 alcohol with a 20% selectivity and a 10.8% PCE. DFT simulations suggest that the interfaces between the Cu(111) and Cu(100) facets can play a role in collocating the key C_3 intermediates. TEM studies correlate HF-Cu with selectivity towards C_3 production. XRD and operando XAS rule out major effects from the Cu atomic environments (oxidation states, coordination or strain). This work offers a clear C_3 active site and formation pathway, which will guide the future design of catalysts that target multicarbon products. Moreover, the strategy is valuable for heterogeneous catalysts more generally, as it combines individual binding sites to facilitate the intermolecular coupling of intermediate species in the synthesis of high-value molecules.

Methods

DFT calculations. In this work, all the DFT calculations were carried out with a periodic slab model using the Vienna ab initio simulation program[43–46]. The generalized gradient approximation was used with the Perdew-Burke-Ernzerhof[47] exchange-correlation functional. The projector-augmented wave method[48,49] was utilized to describe the electron–ion interactions, and the cut-off energy for the plane-wave basis set was 450 eV. To illustrate the long-range dispersion interactions between the adsorbates and catalysts, we employed the D3 correction method of Grimme et al[50]. Brillouin zone integration was accomplished using a $3\times3\times1$ Monkhorst-Pack *k*-point mesh. All the adsorption geometries were optimized using a force-based conjugate gradient algorithm, and transition states were located with a constrained minimization technique[51–53]. At all intermediate and transition states, one charged layer of water molecules was added to the surface to take the combined field and solvation effects into account[38]. In the CO dimerization, there is no proton or electron transfer, and thus the computational hydrogen electrode was not used in this work. Atomic coordinates of the optimized computational models are made available in CIF format (Supplementary Data 2–7).

Materials synthesis. CuI, potassium iodide (KI), methanol (≥99.5%), propylene oxide (≥99%) and *N*,*N*-dimethylformamide were purchased from Sigma-Aldrich.

The HF-Cu precatalysts were synthesized using a solution-based technique. CuI (10 mmol) and KI (20 mmol, as a hydrotropic agent) were first dissolved in *N*,*N*-dimethylformamide (30 ml) in a centrifuge tube. Propylene oxide (8.25 ml) and deionized water (1 ml) were added into the solution dropwise under continuous stirring at roughly 500 revolutions per minute. The mixture was stored in air at room temperature for 24 h. As the Cu(I)I precursor was slowly oxidized by the oxygen in air and hydrolysed, a precipitate with a dark brown colour formed at the bottom of the tube. The precipitate was then collected by centrifugation, washed with acetone three times, further dried in a vacuum chamber and ground in an agate mortar before use. Further annealing was performed in a tube furnace under an argon atmosphere.

Preparation of GDEs. GDEs were prepared by loading catalysts onto a Freudenberg gas diffusion layer (Fuel Cell Store) using an airbrush technique. Ink was first prepared by mixing 30 mg of precatalyst (HF-Cu, MF-Cu, LF-Cu or Cu_2O nanoparticles), 120 µl of Nafion solution (5 wt%, Sigma-Aldrich) and 2.5 ml of methanol. The ink was sonicated for 30 min with frequent vortexing before airbrushing. Well-dispersed ink was then airbrushed onto a piece of gas diffusion layer (3.4×5.1 cm^2) using a Paasche double-action airbrush pumped by nitrogen (99.99%, Praxair) at a fixed pressure of 10 p.s.i. An airbrushed gas diffusion layer was dried in a vacuum chamber before use. The loading amount was determined by weighing the gas diffusion layer before and after the airbrushing, and was found to be roughly 0.8 mg cm^{-2}.

The thermal evaporation of copper metal (99.99%) onto the gas diffusion layer was carried out using an Angstrom Nexdep Evaporator. The deposition was performed at ~10^{-5}–10^{-6} torr at 1.5 Å s^{-1}.

CORR on gas diffusion layers. Electroreduction was performed in a flow cell configuration that consisted of a catalyst-deposited GDE as the working electrode, an anion exchange membrane (Fumasep FAA-PK-130) and nickel foam (1.6 mm thickness, MTI Corporation) as the anode. The combined catalyst and diffusion layer, anion exchange membrane and nickel anode were then positioned and clamped together using polytetrafluoroethylene spacers such that a liquid electrolyte could be introduced into the chambers between the anode and membrane as well as between the membrane and cathode. Gaseous CO was then passed behind the gas diffusion layer to diffuse into the liquid electrolyte present at the catalyst. In the catholyte stream, a port drilled into the polytetrafluoroethylene spacer allows an Ag/AgCl reference electrode to be positioned at a specific distance from the working electrode. All the electrochemical experiments were performed using an electrochemical workstation (Autolab PGSTAT302N) with an Ag/AgCl reference (with 1 M KCl as the filling solution). Electrode potentials were rescaled to the RHE reference by:

$$E\ (\text{versus RHE}) = E\ (\text{versus Ag/AgCl}) + 0.235\ V + 0.0591\times\text{pH} \quad (1)$$

The electrolyte (1 M KOH solution, 8 ml for each of the catholyte and anolyte) was circulated through the electrochemical cell using peristaltic pumps with silicone Shore A50 tubing. The electrolyte flow was keep at 10 ml min^{-1}. The CO (Praxair, 99.8%) flow was kept constant at 50 m min^{-1} using a mass flow controller. The reactions were run for at least 10 min before the liquid and gas products were collected for analysis.

To measure the cell resistance, we performed an electrochemical impedance spectroscopy measurement using an Autolab PGSTAT302N electrochemical workstation, and obtained a cell resistance R_{cell} of 2.58 Ω, consistent with our previous measurements[41]. We then performed *iR* correction using the equation:

$$E_{cat} = E_{applied} - 0.85 I_{total} R_{cell} \quad (2)$$

Where E_{cat} is the corrected potential at the cathode, $E_{applied}$ is the applied potential reported in Fig. 4, and I_{total} is the total current (a negative value at the cathode). A factor of 0.85 is used for the correction term because the 1 M KOH electrolyte has a low resistivity and holds a relatively low voltage drop over the electrolyte.

Product detection. The gas products from CORR (H_2 and C_2H_4, with no CH_4 reliably detected as a gas product) were analysed using a gas chromatograph (PerkinElmer Clarus 680) coupled with a thermal conductivity detector and a flame ionization detector. The gas chromatograph was equipped with a Molecular Sieve 5A and Carboxen-1000 packed columns. Argon (Linde, 99.999%) was used as the carrier gas.

The liquid products were quantified using NMR spectroscopy. ^{1}H NMR spectra of freshly acquired samples were collected on an Agilent DD2 500 spectrometer in 10% D_2O using the water suppression mode, with dimethyl sulfoxide as the internal standard. A relaxation time between the pulses of 16 s was used to allow for complete proton relaxation.

Characterization. XAFS spectra were collected at the 20-BM-B beamline of the Advanced Photon Source located at the Argonne National Laboratory. Cu K-edge XAFS spectra were recorded using a fluorescence mode with an associated energy resolution ($\Delta E/E$) of 1.4×10^{-4}. During the in situ synchrotron characterization, a similar flow cell electrolyser to that described above was mounted at the beamline endstation, which formed a triangle geometry with incident X-rays and a fluorescence detector. Note that an open design of the gas compartment was made in our in situ flow cell where the backside of the GDE was exposed outward, and an X-ray transparent Kapton tape was used to seal the gas compartment by enabling a continuous gas flow. During the in situ experiment, an X-ray with an incident angle of 45° reached the backside of the GDE through the Kapton layer and a fluorescence detector with an angle of 90° to the incident beam was set at the same side to compile the fluorescence signal. A Cu foil was measured for energy calibration and all the XAFS spectra were normalized to the incident photon flux.

DF-TEM and HR-TEM images were recorded using Hitachi 3300 F electron microscopes and under 300 kV operation condition. ADF-STEM imaging was performed on various samples in a Cs-corrected STEM (JEOL, JEM-ARM200F) at an accelerating voltage of 200 kV.

Image processing. DF-TEM images were processed in image processing software ImageJ. All the images were added to a stack and processed with exactly the same steps, with background suppression and brightness thresholding with a software-chosen threshold using built-in routines of the software. Finally, the built-in particle analysis routine was used to extract the particle size information.

Calculation of the thermal equilibrium potential for CO to *n*-propanol conversion and electrical PCE. PCE was calculated using the formula:

$$\text{PCE} = \text{FE}\frac{E_{0,an} - E_{0,cat}}{E_{0,an} - E_{0,cat} + \eta_{an} + \eta_{cat}} \quad (3)$$

where $E_{0,an}$ and $E_{0,cat}$ are the thermal equilibrium potential at the anode and the cathode, and η_{an} and η_{cat} are the overpotential at the anode and the cathode. $E_{0,an} = 1.23$ V versus RHE for the oxygen evolution reduction (OER). $E_{0,cat}$ for the CO to 1-propanol conversion is determined to be 0.203 V versus RHE using a published method[28] and published values of the standard molar Gibbs energy of formation[54,55]. $E_{0,cat} = 0.21$ V versus RHE for the CO_2 to 1-propanol conversion[15]. η_{an} is assumed using the lowest value achieved in the literature for a neutral OER[56], which corresponds to CO_2RR, and a basic OER[57], which corresponds to CORR.

Data availability

The data that support the findings of this study are available from the corresponding author on reasonable request.

Received: 5 May 2018; Accepted: 31 December 2018;
Published online: 11 February 2019

References

1. Won, D. H. et al. Highly efficient, selective, and stable CO_2 electroreduction on a hexagonal Zn catalyst. *Angew. Chem. Int. Ed.* **55**, 9297–9300 (2016).
2. Ma, M., Trześniewski, B. J., Xie, J. & Smith, W. A. Selective and efficient reduction of carbon dioxide to carbon monoxide on oxide-derived nanostructured silver electrocatalysts. *Angew. Chem. Int. Ed.* **55**, 9748–9752 (2016).
3. Liu, M. et al. Enhanced electrocatalytic CO_2 reduction via field-induced reagent concentration. *Nature* **537**, 382–386 (2016).
4. Verma, S. et al. Insights into the low overpotential electroreduction of CO_2 to CO on a supported gold catalyst in an alkaline flow electrolyzer. *ACS Energy Lett.* **3**, 193–198 (2017).
5. Dai, L. et al. Ultrastable atomic copper nanosheets for selective electrochemical reduction of carbon dioxide. *Sci. Adv.* **3**, e1701069 (2017).
6. Gao, S. et al. Ultrathin Co_3O_4 layers realizing optimized CO_2 electroreduction to formate. *Angew. Chem. Int. Ed.* **55**, 698–702 (2016).
7. Wang, Y., Zhou, J., Lv, W., Fang, H. & Wang, W. Electrochemical reduction of CO_2 to formate catalyzed by electroplated tin coating on copper foam. *Appl. Surf. Sci.* **362**, 394–398 (2016).
8. Klinkova, A. et al. Rational design of efficient palladium catalysts for electroreduction of carbon dioxide to formate. *ACS Catal.* **6**, 8115–8120 (2016).
9. Zheng, X. et al. Sulfur-modulated tin sites enable highly selective electrochemical reduction of CO_2 to formate. *Joule* **1**, 794–805 (2017).
10. De Luna, P. et al. Catalyst electro-redeposition controls morphology and oxidation state for selective carbon dioxide reduction. *Nat. Catal.* **1**, 103–110 (2018).
11. Mistry, H. et al. Highly selective plasma-activated copper catalysts for carbon dioxide reduction to ethylene. *Nat. Commun.* **7**, 12123 (2016).
12. Pang, Y. et al. Joint tuning of nanostructured Cu-oxide morphology and local electrolyte programs high-rate CO_2 reduction to C_2H_4. *Green Chem.* **19**, 4023–4030 (2017).
13. Ma, S. et al. One-step electrosynthesis of ethylene and ethanol from CO_2 in an alkaline electrolyzer. *J. Power Sources* **301**, 219–228 (2016).
14. Ma, S. et al. Electroreduction of carbon dioxide to hydrocarbons using bimetallic Cu–Pd catalysts with different mixing patterns. *J. Am. Chem. Soc.* **139**, 47–50 (2016).
15. Kuhl, K. P., Cave, E. R., Abram, D. N. & Jaramillo, T. F. New insights into the electrochemical reduction of carbon dioxide on metallic copper surfaces. *Energy Environ. Sci.* **5**, 7050–7059 (2012).
16. Loiudice, A. et al. Tailoring copper nanocrystals towards C_2 products in electrochemical CO_2 reduction. *Angew. Chem. Int. Ed.* **55**, 5789–5792 (2016).
17. Papa, A. J. in *Ullmann's Encyclopedia of Industrial Chemistry* (eds Elvers, B. et al.) 243–254 (Wiley, Weinheim, 2000).
18. Hori, Y., Murata, A., Takahashi, R. & Suzuki, S. Enhanced formation of ethylene and alcohols at ambient temperature and pressure in electrochemical reduction of carbon dioxide at a copper electrode. *J. Chem. Soc. Chem. Comm.* **1**, 17–19 (1988).
19. Ren, D., Wong, N. T., Handoko, A. D., Huang, Y. & Yeo, B. S. Mechanistic insights into the enhanced activity and stability of agglomerated Cu nanocrystals for the electrochemical reduction of carbon dioxide to *n*-propanol. *J. Phys. Chem. Lett.* **7**, 20–24 (2015).
20. Kim, D., Kley, C. S., Li, Y. & Yang, P. Copper nanoparticle ensembles for selective electroreduction of CO_2 to C_2-C_3 products. *Proc. Natl Acad. Sci. USA* **114**, 10560–10565 (2017).
21. Rahaman, M., Dutta, A., Zanetti, A. & Broekmann, P. Electrochemical reduction of CO_2 into multicarbon alcohols on activated Cu mesh catalysts: an identical location (IL) study. *ACS Catal.* **7**, 7946–7956 (2017).
22. Jiang, K. et al. Metal ion cycling of Cu foil for selective C–C coupling in electrochemical CO_2 reduction. *Nat. Catal.* **1**, 111–119 (2018).
23. Zhuang, T. T. et al. Steering post-C–C coupling selectivity enables high efficiency electroreduction of carbon dioxide to multi-carbon alcohols. *Nat. Catal.* **1**, 421–428 (2018).
24. Kortlever, R., Shen, J., Schouten, K. J. P., Calle-Vallejo, F. & Koper, M. T. Catalysts and reaction pathways for the electrochemical reduction of carbon dioxide. *J. Phys. Chem. Lett.* **6**, 4073–4082 (2015).
25. Ou, L., Long, W., Chen, Y. & Jin, J. New reduction mechanism of CO dimer by hydrogenation to C_2H_4 on a Cu(100) surface: theoretical insight into the kinetics of the elementary steps. *RSC Adv.* **5**, 96281–96289 (2015).
26. Xiao, H., Cheng, T., Goddard, W. A. III & Sundararaman, R. Mechanistic explanation of the pH dependence and onset potentials for hydrocarbon products from electrochemical reduction of CO on Cu(111). *J. Am. Chem. Soc.* **138**, 483–486 (2016).
27. Birat, J. P. & Maizières-lès-Metz, D. *Global Technology Roadmap for CCS in Industry—Steel Sectorial Report* (UNIDO Global Technology Roadmap for CCS in Industry—Sectoral Experts Meeting, Amsterdam, 2010.)
28. Li, C. W., Ciston, J. & Kanan, M. W. Electroreduction of carbon monoxide to liquid fuel on oxide-derived nanocrystalline copper. *Nature* **508**, 504–507 (2014).
29. Verdaguer-Casadevall, A. et al. Probing the active surface sites for CO reduction on oxide-derived copper electrocatalysts. *J. Am. Chem. Soc.* **137**, 9808–9811 (2015).
30. Raciti, D. et al. Low-overpotential electroreduction of carbon monoxide using copper nanowires. *ACS Catal.* **7**, 4467–4472 (2017).
31. Bertheussen, E. et al. Acetaldehyde as an intermediate in the electroreduction of carbon monoxide to ethanol on oxide-derived copper. *Angew. Chem. Int. Ed.* **55**, 1450–1454 (2016).
32. Jouny, M., Luc, W. & Jiao, F. High-rate electroreduction of carbon monoxide to multi-carbon products. *Nat. Catal.* **1**, 748–755 (2018).
33. Zhuang, T. T. et al. Copper nanocavities confine intermediates for efficient electrosynthesis of C_3 alcohol fuels from carbon monoxide. *Nat. Cat.* **1**, 946–951 (2018).
34. Li, J. et al. Copper adparticle enabled selective electrosynthesis of *n*-propanol. *Nat. Commun.* **9**, 4614 (2018).
35. Feng, X., Jiang, K., Fan, S. & Kanan, M. W. A direct grain-boundary-activity correlation for CO electroreduction on Cu nanoparticles. *ACS Cent. Sci.* **2**, 169–174 (2016).
36. Cheng, T., Xiao, H. & Goddard, W. A. Nature of the active sites for CO reduction on copper nanoparticles; suggestions for optimizing performance. *J. Am. Chem. Soc.* **139**, 11642–11645 (2017).
37. Xiao, H., Cheng, T. & Goddard, W. A. Atomistic mechanisms underlying selectivities in C_1 and C_2 products from electrochemical reduction of CO on Cu(111). *J. Am. Chem. Soc.* **139**, 130–136 (2017).
38. Montoya, J. H., Shi, C., Chan, K. & Nørskov, J. K. Theoretical insights into a CO dimerization mechanism in CO_2 electroreduction. *J. Phys. Chem. Lett.* **6**, 2032–2037 (2015).
39. Zhuang, T. T. et al. Controlled synthesis of kinked ultrathin ZnS nanorods/nanowires triggered by chloride ions: a case study. *Small* **10**, 1394–1402 (2014).
40. Lee, S., Kim, D. & Lee, J. Electrocatalytic production of C_3–C_4 compounds by conversion of CO_2 on a chloride-induced bi-phasic Cu_2O–Cu catalyst. *Angew. Chem. Int. Ed.* **54**, 14701–14705 (2015).
41. Dinh, C. T. et al. Selective CO_2 electroreduction to ethylene via hydroxide-mediated copper catalysis at an abrupt interface. *Science* **360**, 783–787 (2018).
42. Mariano, R. G., McKelvey, K., White, H. S. & Kanan, M. W. Selective increase in CO_2 electroreduction activity at grain-boundary surface terminations. *Science* **358**, 1187–1192 (2017).
43. Kresse, G. & Furthmüller, J. Efficient iterative schemes for ab initio total-energy calculations using a plane-wave basis set. *Phys. Rev. B* **54**, 11169–11186 (1996).
44. Kresse, G. & Furthmüller, J. Efficiency of ab-initio total energy calculations for metals and semiconductors using a plane-wave basis set. *Comp. Mater. Sci.* **6**, 15–50 (1996).
45. Kresse, G. & Hafner, J. Ab-Initio molecular-dynamics simulation of the liquid–metal amorphous-semiconductor transition in germanium. *Phys. Rev. B* **49**, 14251–14269 (1994).
46. Kresse, G. & Hafner, J. Ab initio molecular dynamics for liquid metals. *Phys. Rev. B* **47**, 558–561 (1993).
47. Perdew, J. P., Burke, K. & Ernzerhof, M. Generalized gradient approximation made simple. *Phys. Rev. Lett.* **77**, 3865–3868 (1996).
48. Kresse, G. & Joubert, D. From ultrasoft pseudopotentials to the projector augmented-wave method. *Phys. Rev. B* **59**, 1758–1775 (1999).
49. Blöchl, P. E. Projector augmented-wave method. *Phys. Rev. B* **50**, 17953–17979 (1994).
50. Grimme, S., Antony, J., Ehrlich, S. & Krieg, H. A consistent and accurate ab initio parametrization of density functional dispersion correction (DFT-D) for the 94 elements H–Pu. *J. Chem. Phys.* **132**, 154104 (2010).
51. Michaelides, A. et al. Identification of general linear relationships between activation energies and enthalpy changes for dissociation reactions at surfaces. *J. Am. Chem. Soc.* **125**, 3704–3705 (2003).
52. Liu, Z. P. & Hu, P. General rules for predicting where a catalytic reaction should occur on metal surfaces: a density functional theory study of C–H and C–O bond breaking/making on flat, stepped, and kinked metal surfaces. *J. Am. Chem. Soc.* **125**, 1958–1967 (2003).
53. Alavi, A., Hu, P. J., Deutsch, T., Silvestrelli, P. L. & Hutter, J. CO oxidation on Pt(111): an ab initio density functional theory study. *Phys. Rev. Lett.* **80**, 3650–3653 (1998).
54. Rumble, J. R. *CRC Handbook of Chemistry and Physics* 99th edn, Section 5 (CRC Press, 2018).
55. Speight, J. G. *Lange's Handbook of Chemistry* 16th edn, Section 6 (McGraw-Hill Companies New York, 2005).
56. Zheng, X. et al. Theory-driven design of high-valence metal sites for water oxidation confirmed using in situ soft X-ray absorption. *Nat. Chem.* **10**, 149 (2018).
57. Zhou, H. et al. Water splitting by electrolysis at high current density under 1.6 volt. *Energy Environ. Sci.* **11**, 2858–2864 (2018).

Acknowledgements

This work was supported by the Ontario Research Fund Research-Excellence Program, the Natural Sciences and Engineering Research Council (NSERC) of Canada, the CIFAR Bio-Inspired Solar Energy programme, and the University of Toronto Connaught Program. This research used synchrotron resources of the Advanced Photon Source, an Office of Science User Facility operated for the US Department of Energy (DOE) Office of Science by the Argonne National Laboratory, and was supported by the US DOE under contract no. DE-AC02-06CH11357, and the Canadian Light Source and its funding partners. The authors thank Z. Finfrock and M. J. Ward for technical support at the Sector 20BM beamline. D.S. acknowledges the NSERC E.W.R. Steacie Memorial Fellowship. J.L. acknowledges the Banting Postdoctoral Fellowships program. All DFT computations were performed on the IBM BlueGene/Q supercomputer with support from the Southern Ontario Smart Computing Innovation Platform (SOSCIP). SOSCIP is funded by the Federal Economic Development Agency of Southern Ontario, the Province of Ontario, IBM Canada, Ontario Centres of Excellence, Mitacs and 15 Ontario academic member institutions.

Author contributions

E.H.S. and D.S. supervised the project. Y.P. and J.L. designed the CORR experiments. Y.P., J.L., T.-T.Z., X.W. and Y.X. carried out the CORR experiments. P.D.L. assisted the catalyst preparation. J.L. carried out the operando XAS characterization. Z.W. performed the DFT calculations. C.-S.T., P.-L.H. and L.-J.C. carried out TEM imaging. Y.P., Y. L. and D.W. performed the TEM analysis. Y.P., J.L., Z.-Q.L, C.Z., J.P.E., C.-T.D., F.L. and M.Z. carried out the product detection via NMR and gas chromatography. Z.-Q.L. carried out the XRD characterization. All the authors discussed the results and assisted during manuscript preparation.

Competing interests

The authors declare no competing interests.

Additional information

Supplementary information is available for this paper at https://doi.org/10.1038/s41929-019-0225-7.

Reprints and permissions information is available at www.nature.com/reprints.

Correspondence and requests for materials should be addressed to E.H.S. or D.S.

Publisher's note: Springer Nature remains neutral with regard to jurisdictional claims in published maps and institutional affiliations.